energies

MDPI

Article

Vanadium-Doped Bi_2S_3@$Co_{1-x}S$ Heterojunction Nanofibers as High-Capacity and Long-Cycle-Life Anodes

Haomiao Yang, Lehao Liu, Zhuoheng Wu, Jinkui Zhang, Chenhui Song and Yingfeng Li *

School of New Energy, North China Electric Power University, Beijing 102206, China; yanghmncepu@163.com (H.Y.); lehaoliu@ncepu.edu.cn (L.L.); wuzhuoheng_ncepu@163.com (Z.W.); jkzhangncepu@163.com (J.Z.); cmadoka990@163.com (C.S.)
* Correspondence: liyingfeng@ncepu.edu.cn

Abstract: Lithium-ion batteries (LIBs) are considered one of the most important solutions for energy storage; however, conventional graphite anodes possess limited specific capacity and rate capability. Bismuth sulfide (Bi_2S_3) and cobalt sulfide ($Co_{1-x}S$) with higher theoretical capacities have emerged as promising alternatives, but they face challenges such as significant volume expansion during electrochemical cycling and poor electrical conductivity. To tackle these problems, vanadium was doped into Bi_2S_3 to improve its electronic conductivity; subsequently, a vanadium-doped Bi_2S_3 (V-Bi_2S_3)@$Co_{1-x}S$ heterojunction structure was synthesized via a facile hydrothermal method to mitigate volume expansion by the closely bonded heterojunction interface. Moreover, the built-in electric field (BEF) created at the heterointerfaces can significantly enhance charge transport and facilitate reaction kinetics. Additionally, the nanofiber morphology of the V-Bi_2S_3@$Co_{1-x}S$ heterojunction structure further contributed to improved electrochemical performance. As a result, the V-Bi_2S_3 electrode exhibited better electrochemical performance than the pure Bi_2S_3 electrode, and the V-Bi_2S_3@$Co_{1-x}S$ electrode showed a significantly enhanced performance compared to the V-Bi_2S_3 electrode. The V-Bi_2S_3@$Co_{1-x}S$ heterojunction electrode displayed a high capacity of 412.5 mAh g^{-1} after 2000 cycles at 1.0 A g^{-1} with high coulombic efficiencies of ~100%, indicating a remarkable long-term cycling stability.

Keywords: vanadium doping; heterojunction; V-Bi_2S_3@$Co_{1-x}S$ nanofiber; lithium-ion batteries

Citation: Yang, H.; Liu, L.; Wu, Z.; Zhang, J.; Song, C.; Li, Y. Vanadium-Doped Bi_2S_3@$Co_{1-x}S$ Heterojunction Nanofibers as High-Capacity and Long-Cycle-Life Anodes. *Energies* **2024**, *17*, 6196. https://doi.org/10.3390/en17236196

Academic Editor: Ohbyong Chae

Received: 21 November 2024
Revised: 5 December 2024
Accepted: 6 December 2024
Published: 9 December 2024

1. Introduction

Lithium-ion batteries (LIBs) play a crucial role in avoiding excessive consumption of fossil fuels, and are widely used for energy storage [1,2]. However, graphite as a commercialized anode material of LIBs cannot well meet the demands of next-generation LIBs due to its limited specific capacity (372 mAh g^{-1}) and poor rate capability [3]. Metal sulfides (MSs) have garnered significant attention as promising negative electrode materials for LIBs because of their high theoretical capacities, higher Li^+ diffusion coefficients, and abundant active sites compared to conventional graphite-based anodes [4]. Among them, bismuth sulfide (Bi_2S_3) has attracted significant interest as a potential anode material for LIBs due to its exceptional theoretical specific capacity of 625 mAh g^{-1} based on the conversion reaction mechanism, significantly surpassing the capacity of traditional graphite anodes [5]. Unfortunately, challenges remain in terms of MSs' large volume expansion during lithiation, which leads to poor cyclability over repeated charge/discharge cycles [6]. Additionally, low electrical conductivity also limits their broad utilization [7].

To tackle these challenges, various strategies have been proposed to improve electrochemical performance [5,8]. Among these, the design of nanostructure has been put forward to improve electrochemical performance, and the incorporation of heterostructure into electrode materials stands out as particularly effective [9,10]. The reduced dimensions of nanosized structure can facilitate fast kinetics and high charge/discharge

rates, and the increased surface area enables higher capacity [11]. The introduction of heterostructure creates a built-in electric field (BEF) at the heterointerfaces, which significantly facilitates reaction kinetics and enhances charge transfer in LIBs [12]. Moreover, the closely bonded heterojunction interface between different phases also alleviates the volumetric change in each constituent material [13]. This design strategy not only increases the cycling stability of the electrode, but also enhances its rate capability. For example, heterostructured MoS_2/MnS/SnS trimetallic sulfides were successfully coated with N-doped carbon nanorods (MMSS@NC), which were designed to improve ionic and electronic diffusion kinetics and maintain structural stability during the repeated lithiation/delithiation process [14]. The 2D-layered SnS_2/MoS_2 heterostructured composites, by combining SnS_2 and MoS_2 in different ratios, were also synthesized through a simple hydrothermal method, which can effectively enhance electrochemical kinetics and mitigate volume change issues as anodes in LIBs [15].

Another crucial method for enhancing electrochemical performance involves cation doping, which is widely recognized for its effectiveness in improving the electronic conductivity of electrode materials [16,17]. For example, the optimal composition of $TiNb_{1.98}V_{0.02}O_7$ exhibits outstanding electrochemical performance, achieving a reversible capacity improvement exceeding 50 mAh g^{-1} compared to un-doped $TiNb_2O_7$ [18]. However, to the best our knowledge, none of these methods have been used to improve the electrochemical performance of MSs, and vanadium-doped Bi_2S_3 (V-Bi_2S_3) has never been reported before.

In this study, we synthesized V-Bi_2S_3 nanofibers via a facile hydrothermal method for the first time. Subsequently, V-Bi_2S_3@$Co_{1-x}S$ composite nanofibers with heterojunction were prepared through the in situ growth of $Co_{1-x}S$ on the V-Bi_2S_3 nanofibers by the hydrothermal synthesis process once again (Figure 1). X-ray photoelectron spectroscopy (XPS) and high-resolution transmission electron microscopy (HRTEM) confirmed the existence of a thin heterointerface between V-Bi_2S_3 and $Co_{1-x}S$. The remarkable electrochemical performances of V-Bi_2S_3@$Co_{1-x}S$ are attributed to doping and the formation of heterojunctions. As anticipated, the V-Bi_2S_3 electrode demonstrated superior electrochemical performance compared to the pure Bi_2S_3 electrode. Furthermore, the V-Bi_2S_3@$Co_{1-x}S$ electrode exhibited significantly enhanced performance compared to the V-Bi_2S_3 electrode, maintaining a high capacity of 412.5 mAh g^{-1} even after 2000 cycles at 1.0 A g^{-1}, with nearly 100% coulombic efficiencies. This paper introduces an innovative approach to enhance the electrochemical performance of anode materials for LIBs.

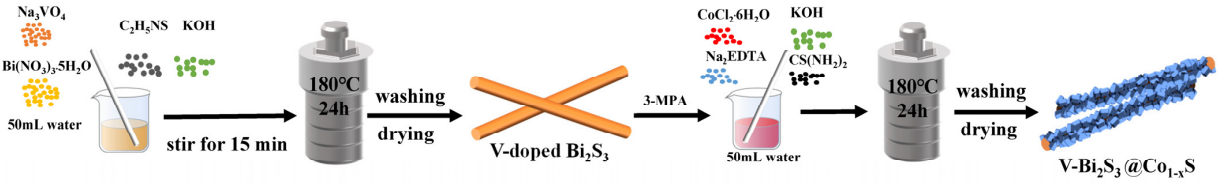

Figure 1. Schematic illustration of fabrication of V-Bi_2S_3@$Co_{1-x}S$ heterojunction nanofibers as anode materials.

2. Materials and Methods

2.1. Preparation of Bi_2S_3 and V-Bi_2S_3 Samples

An appropriate amount of $Bi(NO_3)_3 \cdot 5H_2O$ was dissolved in 50 mL of distilled water. Subsequently, Na_3VO_4 with a molar ratio with $Bi(NO_3)_3 \cdot 5H_2O$ of 3:1 was added. And the mixture was stirred magnetically. Next, 0.005 mol of C_2H_5NS and 0.025 mol of KOH were added to the solution, which was stirred for 15 min. The mixture was transferred into a 100 mL Teflon-lined autoclave, sealed, heated to 180 °C, and maintained for 24 h. After the hydrothermal process, the products were filtered, washed with distilled water and ethanol several times, and then dried at 70 °C for 6 h to obtain the V-Bi_2S_3 sample.

Pure Bi_2S_3 was also synthesized with a similar procedure as for the V-Bi_2S_3, without the addition of Na_3VO_4.

2.2. Preparation of V-Bi_2S_3@$Co_{1-x}S$ Heterojunction Nanofiber

First, 80 mg of V-Bi_2S_3 was mixed with a solution consisting of 25 mL of distilled water and 80 µL of 3-mercaptopropionic acid (3-MPA). The mixture was sonicated for 10 min and magnetically stirred for 2 h, and then centrifuged at 7200 rpm for 12 min to remove excess 3-MPA. Next, 0.595 g of $CoCl_2 \cdot 6H_2O$ was dissolved in 50 mL of distilled water, followed by the addition of disodium ethylenediamine tetraacetate (Na_2EDTA), heated, and stirred at 60 °C until the solution was clear. Subsequently, 0.381 g of thiourea ($CS(NH_2)_2$), 1.403 g of KOH, and the V-Bi_2S_3 combined with 3-MPA were added to the clear solution and stirred magnetically for 15 min. The final mixture was put in a Teflon-lined autoclave and heated at 180 °C for 24 h, followed by natural cooling to room temperature. After that, the product was filtered, cleaned several times with pure water and ethanol, and desiccated at 70 °C for 8 h to obtain the V-Bi_2S_3@$Co_{1-x}S$ sample.

2.3. Material Characterization

An X-ray diffractometer (XRD, D8 focus, Bruker Corporation, Billerica, MA, USA) with Cu Kα radiation was used to analyze the crystal structures. The chemical composition and heterojunction characteristics were investigated by X-ray photoelectron spectroscopy (XPS, ESCALAB 250Xi, Thermo Fisher Scientific, Waltham, MA, USA) with Al Kα radiation. The morphology and microstructure of the samples were characterized using a scanning electron microscope (SEM, Apreo 2C, Thermo Fisher Scientific, Waltham, MA, USA) and a transmission electron microscope (TEM, Talos F200S, Thermo Fisher Scientific, Waltham, MA, USA) with an energy-dispersive X-ray spectrometer.

2.4. Electrochemical Measurements

Electrochemical performances were tested by assembling CR2032 coin-type cells in an argon-filled glovebox. The as-synthesized materials, conductive agent (acetylene black), and polyvinylidene fluoride (PVDF) were mixed in a weight ratio of 7:2:1, and then a slurry was formed by the addition of N-methyl-pyrrolidone (NMP), which was then coated onto copper foil. And the slurry was dried under vacuum at 110 °C overnight. Here, the polypropylene membrane was used as a separator, and the mass loading of the active material on each electrode was approximately 1.2 mg cm^{-2}. The electrolyte consisted of 1.0 M $LiPF_6$ dissolved in a solvent mixture of ethylene carbonate (EC), dimethyl carbonate (DMC), and ethyl methyl carbonate (EMC) in a volume ratio of 1:1:1. A CT2001A battery-testing instrument (LAND Electronic Co., Wuhan, China) was used to conduct galvanostatic discharge/charge tests. Cyclic voltammetry (CV) profiles and electrochemical impedance spectra (EIS) measurements were obtained using an electrochemical workstation (VMP3, Bio-Logic, Grenoble, France), and CV measurements were performed at 0.2 mV s^{-1} within a voltage range of 0.01–3.0 V; EIS tests were obtained over a frequency range of 1000 kHz to 10 mHz, with a potential of 5 mV.

3. Results and Discussion

3.1. Characterization of V-Bi_2S_3 Nanofiber

Figure 2a shows the XRD patterns of the V-Bi_2S_3 sample, in which all diffraction peaks correspond to the orthorhombic phase of Bi_2S_3 (JCPDS card, No: 17-0320), and no impurity peaks are observed, indicating successful V doping into Bi_2S_3 [19]. And the microstructures of V-Bi_2S_3 and Bi_2S_3 samples are shown in Figure 2b and Figure S1, displaying a uniform microstructure of nanofibers. Moreover, as shown in Figure 2c, element-mapping images demonstrate that Bi, V, and S elements were evenly distributed in the V-Bi_2S_3 sample, which further shows V-Bi_2S_3 that was successfully prepared [20]. In addition, the EDS spectra of the V-Bi_2S_3 sample are shown in Figure S2, which confirm the existence of V, Bi, and S elements, also evidencing successful V doping into Bi_2S_3.

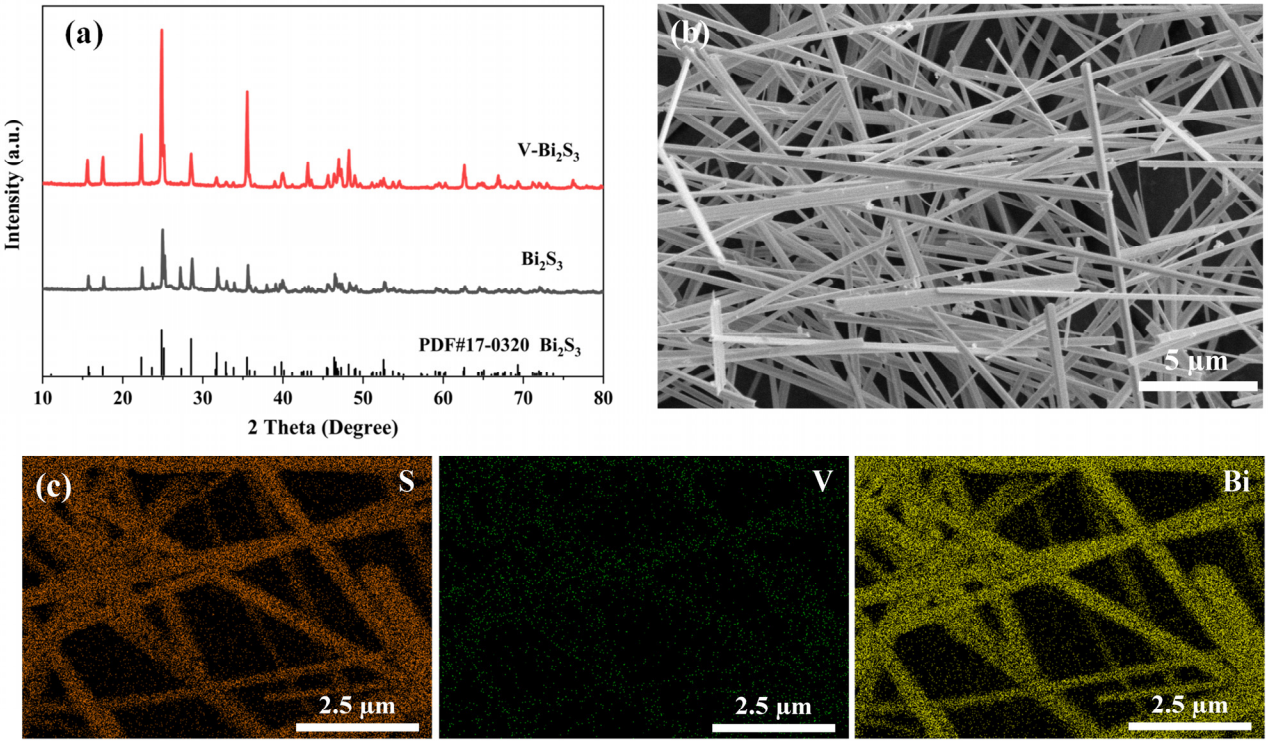

Figure 2. (**a**) XRD patterns; (**b**) SEM image; and (**c**) element mapping images of V-Bi_2S_3 sample.

3.2. Characterization of V-Bi_2S_3@$Co_{1-x}S$ Heterojunction Nanofiber

The XRD patterns of V-Bi_2S_3@$Co_{1-x}S$ heterojunction nanofiber are presented in Figure 3a, in which the diffraction peaks of V-Bi_2S_3 correspond to Bi_2S_3 (JCPDS card, No: 17-0320), and the three strong peaks at 2 theta of 24.9°, 25.2°, and 28.6° are attributed to the (130), (310), and (211) crystal planes of Bi_2S_3, respectively. In addition, the newly formed peaks at 30.5°, 35.1°, and 46.7° are assigned to the (100), (101), and (102) crystal planes of hexagonal $Co_{1-x}S$ (JCPDS Card, No: 42-0826), respectively, suggesting the formation of V-Bi_2S_3@$Co_{1-x}S$.

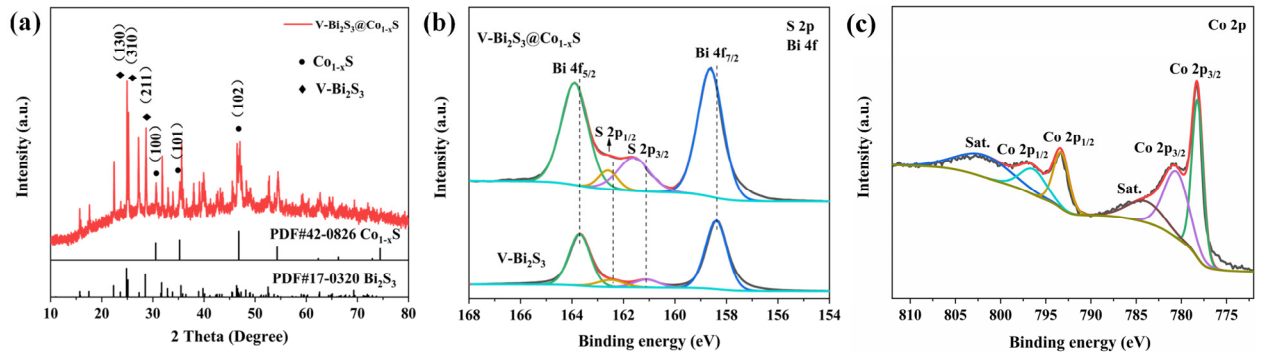

Figure 3. (**a**) XRD patterns of V-Bi_2S_3@$Co_{1-x}S$ sample; (**b**) high-resolution XPS spectra of S 2p and Bi 4f in V-Bi_2S_3@$Co_{1-x}S$ and V-Bi_2S_3; and (**c**) high-resolution XPS spectra of Co 2p in V-Bi_2S_3@$Co_{1-x}S$.

The chemical composition and the formation of heterojunction of the V-Bi_2S_3@$Co_{1-x}S$ sample were confirmed by high-resolution XPS spectra of Bi and S elements, as shown in Figure 3b,c. For the V-Bi_2S_3@$Co_{1-x}S$ sample, prominent peaks at 158.6 and 163.9 eV are assigned to Bi 4f7/2 and Bi 4f5/2, while additional weaker peaks centered at 161.6 and 162.6 eV are attributed to S 2p3/2 and S 2p1/2, respectively [21]. Comparatively, the pure V-Bi_2S_3 sample shows similar spectra as the V-Bi_2S_3@$Co_{1-x}S$ sample, but the Bi 4f and S 2p peaks of V-Bi_2S_3@$Co_{1-x}S$ shifted obviously to higher binding energy owing

to the spontaneous formation of heterojunction and the resulting migration of electron cloud density [22]. Figure 3c demonstrates the presence of Co elements with the peaks at 793.3 and 778.2 eV corresponding to Co 2p1/2 and Co 2p3/2 of Co-S, and the peaks at 796.4 and 780.5 eV corresponding to Co 2p1/2 and Co 2p3/2 of Co-O, respectively [23]. These findings confirm the presence of $Co_{1-x}S$ in the V-Bi_2S_3@$Co_{1-x}S$, consistent with the XRD results.

The microstructure of the V-Bi_2S_3@$Co_{1-x}S$ sample was observed by SEM and TEM. The V-Bi_2S_3@$Co_{1-x}S$ sample displays a uniform nanofiber morphology, with a rough surface due to the in situ growth of $Co_{1-x}S$ on the V-Bi_2S_3 nanofibers (Figure 4a,c). As shown in Figure 4b, the EDS spectrum confirms the existence of Co, Bi, V, and S elements within the V-Bi_2S_3@$Co_{1-x}S$ sample. To further confirm the formation of heterojunction and the chemical composition between the two phases, the HRTEM image of the V-Bi_2S_3@$Co_{1-x}S$ nanofiber is presented in Figure 4d. The lattice fringes with d-spacings of 0.316 and 0.194 nm correspond to the (211) plane of Bi_2S_3 and the (102) plane of $Co_{1-x}S$, respectively. The $Co_{1-x}S$ phase is in close contact with the Bi_2S_3 phase, indicating the formation of a thin heterojunction interface in the V-Bi_2S_3@$Co_{1-x}S$ nanofiber, as indicated by the red dotted line. Such close linkage at the interface serves a role similar to anchoring, which helps suppress volumetric expansion. Moreover, Figure 4e confirms the uniform distribution of Bi, Co, V, and S elements in the V-Bi_2S_3@$Co_{1-x}S$ heterojunction nanofibers and the $Co_{1-x}S$ coating layer on the V-Bi_2S_3 nanofiber.

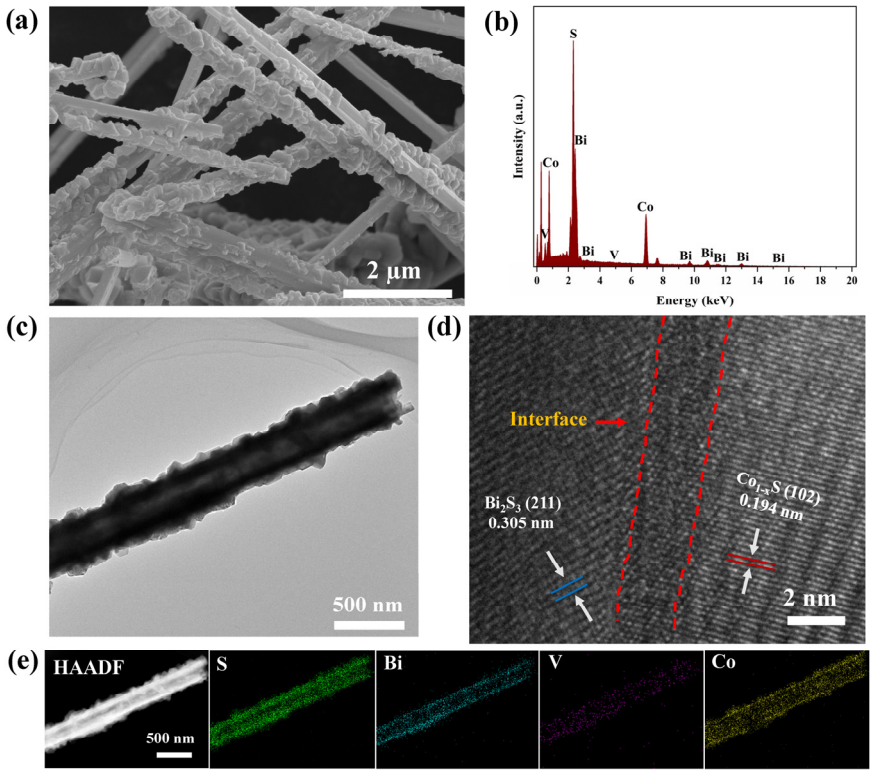

Figure 4. Microstructure of V-Bi_2S_3@$Co_{1-x}S$ nanofibers: (**a**) SEM image; (**b**) EDS spectrum; (**c**) TEM image; (**d**) HRTEM image; and (**e**) elemental mapping analysis of Bi, Co, V, and S elements.

3.3. Electrochemical Performances

CV profiles of the V-Bi_2S_3@$Co_{1-x}S$ electrodes over the first three cycles are presented in Figure 5a. In the initial cathodic scan, four peaks appear, at 1.68, 1.18, 0.75, and 0.67 V. The peak at 1.68 V is related to the reduction of V-Bi_2S_3 metallic Bi and V [24,25]. The peak at 1.18 V is ascribed to the conversion of $Co_{1-x}S$ to metallic Co [6]. The peaks at 0.75 and 0.67 V correspond to the alloying reactions to form LiBi and Li_3Bi, and the formation of a solid electrolyte interface (SEI), respectively [21,26]. During the following charge process, a

strong anodic peak placed at 0.92 V is attributed to the dealloying reaction, and the peak at 2.03 V is assigned to the reformation of V-Bi_2S_3@$Co_{1-x}S$ [24,27]. The oxidation peak at 2.44 V is related to the oxidation reaction from metallic Co to $Co_{1-x}S$ [28].

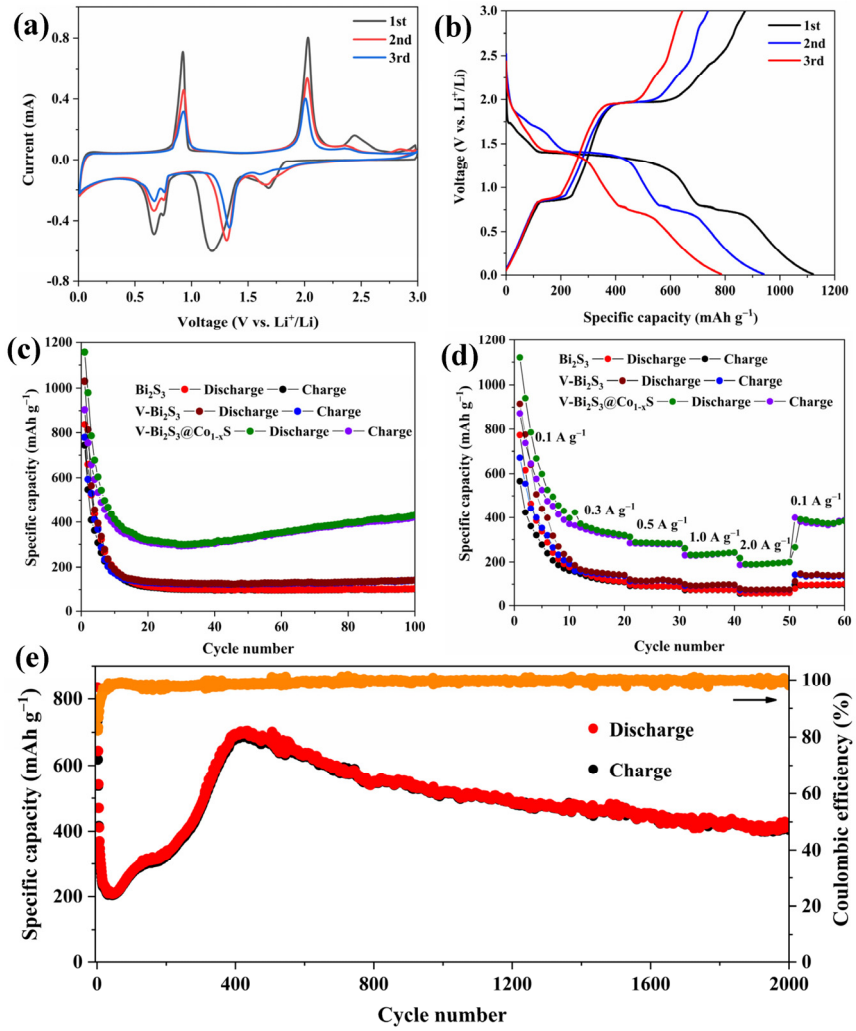

Figure 5. (**a**) Cyclic voltammetry (CV) profiles and (**b**) discharge/charge profiles of the V-Bi_2S_3@$Co_{1-x}S$ electrode at 0.1 A g^{-1} for the first three cycles; (**c**) cycling performance at 0.1 A g^{-1}; (**d**) rate performance of Bi_2S_3, V-Bi_2S_3, and V-Bi_2S_3@$Co_{1-x}S$ electrodes; and (**e**) long-term cycling performance of V-Bi_2S_3@$Co_{1-x}S$ sample at 1.0 A g^{-1}.

The V-Bi_2S_3@$Co_{1-x}S$ electrode was further evaluated by galvanostatic cycling at 0.1 A g^{-1} for the first three cycles (Figure 5b). The voltage platforms in the discharge/charge profiles were basically matched with the abovementioned sharp peaks in the CV curves, revealing the reversible redox processes. The V-Bi_2S_3@$Co_{1-x}S$ electrode delivered high initial discharge and charge capacities of 1120.9 and 872.6 mAh g^{-1} with a coulombic efficiency of 78%, respectively. This initial irreversible capacity was mainly caused by the electrolyte decomposition and the inevitable formation of the SEI film [29]. The galvanostatic discharge/charge profiles of pure V-Bi_2S_3 and Bi_2S_3 electrodes are also shown in Figures S3 and S4 for comparison, and the corresponding discharge and charge specific capacities of the V-Bi_2S_3 and Bi_2S_3 electrodes were only 915.1 and 670.6 mAh g^{-1}, and 773.6 and 566.1 mAh g^{-1}, respectively.

Figure 5c displays the cycling performance of the V-Bi_2S_3@$Co_{1-x}S$, V-Bi_2S_3, and Bi_2S_3 electrodes at 0.1 A g^{-1}. It is obvious that the performance of the V-Bi_2S_3 electrode (142.4 mAh g^{-1} after 100 cycles) was better than that of the Bi_2S_3 electrode (104.7 mAh g^{-1}),

because of the improvement in the electronic conductivity induced by V doping [16,17]. Furthermore, the V-Bi_2S_3@$Co_{1-x}S$ electrode (431.3 mAh g^{-1} after 100 cycles) showed a superior cycling performance compared to that of the V-Bi_2S_3 electrode owing to the formation of heterostructure and the BEF effect. Figure 5d shows that the V-Bi_2S_3@$Co_{1-x}S$ electrode had a much better rate performance than the V-Bi_2S_3 and Bi_2S_3 electrodes. Additionally, as depicted in Figure 5e, the V-Bi_2S_3@$Co_{1-x}S$ electrode displayed outstanding long-term cycling performance. Remarkably, a capacity of 412.5 mAh g^{-1} was maintained even after 2000 cycles at 1.0 A g^{-1} with coulombic efficiencies approaching 100%, which is primarily attributed to the synergistic effects of V doping in Bi_2S_3 and the BEF in the V-Bi_2S_3@$Co_{1-x}S$ heterostructure. During the initial cycles, the capacity of the V-Bi_2S_3@$Co_{1-x}S$ electrode decayed due to electrolyte decomposition and irreversible electrochemical processes, such as the unstable SEI formation. However, the capacity began to increase after several tens of cycles, due to the formation of a stable SEI film and the increased availability of Li^+ for chemical reactions. Furthermore, the heterostructure's ability to alleviate the significant volume change contributed to the cycling stability of the V-Bi_2S_3@$Co_{1-x}S$ electrode [30,31].

The superiority of the V-Bi_2S_3@$Co_{1-x}S$ electrode was further confirmed by electrochemical impedance spectra. As illustrated in Figure 6a, the V-Bi_2S_3 electrode exhibited a smaller semicircle diameter compared to the Bi_2S_3 electrode, indicating that the V-Bi_2S_3 electrode had a much lower charge-transfer resistance due to the improved electronic conductivity from V doping. Moreover, the V-Bi_2S_3@$Co_{1-x}S$ electrode demonstrated the smallest semicircle diameter among the three samples due to the BEF within the heterojunction and the enhanced charge transfer [12,32]. Moreover, the heterostructure can ensure intimate contact between the V-Bi_2S_3 phase and the $Co_{1-x}S$ phase, and mitigate the volumetric change and agglomeration [13], thus enhancing the cycling stability of the electrode. This is evidenced by SEM images of the electrochemically-cycled V-Bi_2S_3 and V-Bi_2S_3@$Co_{1-x}S$ electrodes (Figure 6b,c). In contrast to the pulverization of the V-Bi_2S_3 nanofibers in the V-Bi_2S_3 electrode, the V-Bi_2S_3@$Co_{1-x}S$ sample still maintained the nanofiber structure after long-term cycling.

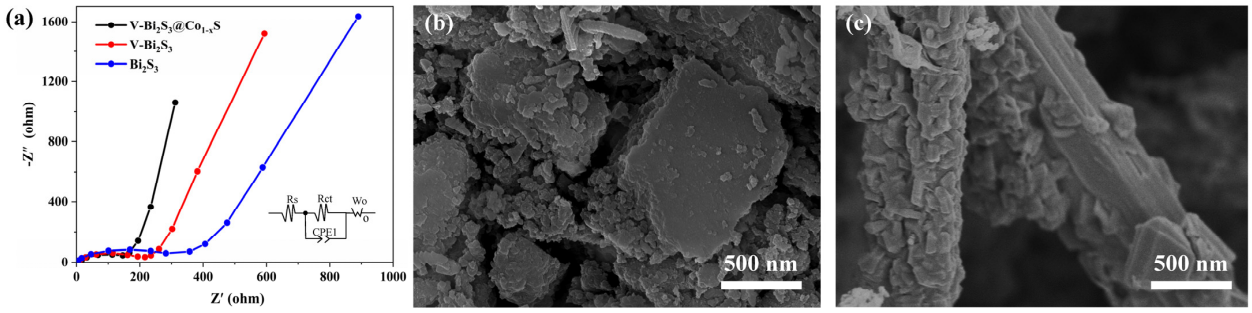

Figure 6. (**a**) EIS electrochemical impedance spectra of V-Bi_2S_3@$Co_{1-x}S$ electrode and SEM images of (**b**) V-Bi_2S_3 and (**c**) V-Bi_2S_3@$Co_{1-x}S$ electrodes after 100 cycles at 0.1 A g^{-1}.

4. Conclusions

In summary, V-Bi_2S_3@$Co_{1-x}S$ heterojunction nanofibers were synthesized using a simple hydrothermal method. V doping enhanced the electronic conductivity of Bi_2S_3. Moreover, the unique heterojunction structure not only facilitated a charge transfer to improve reaction kinetics by creating a built-in electric field, but also mitigated volume change during cycling, both of which were confirmed by the electrochemical impedance spectra and SEM images of the electrochemically cycled electrodes. Therefore, V-Bi_2S_3@$Co_{1-x}S$ showed a significantly enhanced performance compared to the Bi_2S_3 electrode, and it maintained a high capacity of 412.5 mAh g^{-1} even after 2000 cycles at 1.0 A g^{-1} with nearly 100% coulombic efficiencies. This work presents an important strategy for the synthesis of high-capacity anode materials through the integration of doping and heterostructure.

Supplementary Materials: The following supporting information can be downloaded at: https://www.mdpi.com/article/10.3390/en17236196/s1, Figure S1: SEM image of the pure Bi_2S_3 sample; Figure S2: EDS spectra of the V-Bi_2S_3 sample; Figure S3: Charge-discharge curves of the V-Bi_2S_3 fibers as electrode for the first three cycles at 0.1 A g^{-1}; Figure S4: Charge-discharge curves of the Bi_2S_3 sample as electrode for the first three cycles at 0.1 A g^{-1}.

Author Contributions: Conceptualization, H.Y., L.L. and Y.L.; data curation, H.Y.; funding acquisition, L.L. and Y.L.; investigation, H.Y., L.L., Z.W., J.Z., C.S. and Y.L.; methodology, H.Y., L.L. and Y.L.; project administration, L.L.; resources, L.L. and Y.L.; supervision, L.L. and Y.L.; validation, H.Y., Z.W., J.Z. and C.S.; writing—original draft, H.Y. and Z.W.; writing—review and editing, L.L. and Y.L. All authors have read and agreed to the published version of the manuscript.

Funding: This study was supported partially by a project of the National Natural Science Foundation of China (52072121), the Hebei Natural Science Foundation (E2022502022), the State Key Laboratory of Alternate Electrical Power Systems with Renewable Energy Sources (LAPS21004), the China Postdoctoral Science Foundation (2018M631419), Fundamental Research Funds for the Central Universities (2021MS028), and the NCEPU "Double First-Class" Program.

Data Availability Statement: Original contributions of this study are included in this article; further inquiries can be directed to the corresponding author.

Conflicts of Interest: The authors declare no conflicts of interest.

References

1. Dunn, B.; Kamath, H.; Tarascon, J.-M. Electrical energy storage for the grid: A battery of choices. *Science* **2011**, *334*, 928–935. [CrossRef]
2. Zhang, N.X.; Chen, Y.; Yu, M.; Niu, Z.Q.; Cheng, F.Y.; Chen, J. Materials chemistry for rechargeable zinc-ion batteries. *Chem. Soc. Rev.* **2020**, *49*, 4203. [CrossRef]
3. Yu, X.Y.; Yu, L.; Lou, X.W.D. Metal sulfide hollow nanostructures for electrochemical energy storage. *Adv. Energy Mater.* **2016**, *6*, 1501333. [CrossRef]
4. Chen, X.; Liu, Q.; Bai, T.; Wang, W.G.; He, F.L.; Ye, M.D. Nickel and cobalt sulfide-based nanostructured materials for electrochemical energy storage devices. *Chem. Eng. J.* **2021**, *409*, 127237. [CrossRef]
5. Zhang, X.; Xie, J.; Lu, Z.; Liu, X.; Tang, Y.; Wang, Y.; Hu, J.; Cao, Y. Engineering sulfur defective Bi_2S_3@C with remarkably enhanced electrochemical kinetics of lithium-ion batteries. *J. Colloid. Interf. Sci.* **2024**, *667*, 385–392. [CrossRef]
6. Lian, X.T.; Xu, N.; Ma, Y.C.; Hu, F.; Wei, H.X.; Chen, H.Y.; Wu, Y.Z.; Li, L.L.; Li, D.S.; Peng, S.J. In-situ formation of $Co_{1-x}S$ hollow polyhedrons anchored on multichannel carbon nanofibers as self-supporting anode for lithium/sodium-ion batteries. *Chem. Eng. J.* **2021**, *421*, 127755. [CrossRef]
7. Hsu, T.H.; Muruganantham, R.; Liu, W.R. High-energy ball-milling for fabrication of $CuIn_2S_4$/C composite as an anode material for lithium-ion batteries. *Ceram. Int.* **2022**, *48*, 11561–11572. [CrossRef]
8. Park, S.-K.; Woo, S.; Lee, S.; Seong, C.-Y.; Piao, Y.Z. Design and tailoring of three-dimensional graphene-Vulcan carbon-Bi_2S_3 ternary nanostructures for high-performance lithium- ion-battery anodes. *RSC Adv.* **2015**, *5*, 52687–52694. [CrossRef]
9. Liu, X.W.; Li, W.Q.; Zhou, Y.L.; Zhu, D.D.; Chen, X.; Liu, K. Facile one-pot synthesis of Bi_2S_3 nanorod @N, S co-doped carbon composite for high performance lithium ion batteries. *J. Electroanal. Chem.* **2024**, *974*, 118714. [CrossRef]
10. Zhang, H.; Zhao, L.J.; Ye, L.; Li, G.Y. Capacity and cycle performance of lithium ion batteries employing $Co_xZn_{1-x}S/Co_9S_8$@N-doped reduced graphene oxide as anode material. *Chem. Eng. J.* **2021**, *409*, 127372. [CrossRef]
11. AbdelHamid, A.; Mendoza-Garcia, A.; Ying, J. Advances in and prospects of nanomaterials' morphological control for lithium rechargeable batteries. *Nano Energy* **2022**, *93*, 106860. [CrossRef]
12. Zhang, Y.; Wang, P.X.; Yin, Y.Y.; Zhang, X.Y.; Fan, L.S.; Zhang, N.Q.; Sun, K.N. Heterostructured SnS-ZnS@C hollow nanoboxes embedded in graphene for high performance lithium and sodium ion batteries. *Chem. Eng. J.* **2019**, *356*, 1042–1051. [CrossRef]
13. Yin, S.J.; Zhang, X.Q.; Huang, X.X.; Zhou, F.; Wang, Y.S.; Wen, G.W. SnO/SnO_2 heterojunction nanoparticles anchored on graphene nanosheets for lithium storage. *ACS Appl. Nano Mater.* **2024**, *7*, 14419–14430. [CrossRef]
14. Zhang, L.X.; Xie, S.B.; Li, A.Q.; Li, Y.; Zheng, F.H.; Huang, Y.G.; Pan, Q.C.; Li, Q.Y.; Wang, H.Q. Trimetallic sulfides coated with N-doped carbon nanorods as superior anode for lithium-ion batteries. *J. Colloid Inter. Sci.* **2024**, *655*, 643–652. [CrossRef]
15. Venugopal, B.; Mudike, R.; Ravi, R.; Sahoo, P.K.; Tripathi, A.; Shown, I. Harnessing enhanced stability and high-rate capability in lithium-ion batteries using synergistic SnS_2/MoS_2 2D nanostructures with optimized conversion/alloying reactions. *J. Alloy. Compd.* **2024**, *984*, 173886. [CrossRef]
16. Usui, H.; Domi, Y.; Yamamoto, Y.; Hoshi, T.; Tanaka, T.; Oishi, N.; Nitta, N.; Sakaguchi, H. Nickel-doped titanium oxide with layered rock-salt structure for advanced Li-storage materials. *ACS Appl. Electron. Mater.* **2023**, *5*, 6292–6304. [CrossRef]
17. Ma, F.K.; Guan, S.J.; Liu, D.; Liu, Z.M.; Qiu, Y.F.; Sun, C.L.; Wang, Y.J. Ge-doped quaternary metallic oxynitrides GaZnON: The high-performance anode material for lithium-ion batteries. *J. Alloy. Compd.* **2023**, *940*, 168777. [CrossRef]

18. Wen, X.Y.; Ma, C.X.; Du, C.Q.; Liu, J.; Zhang, X.H.; Qu, D.Y.; Tang, Z.Y. Enhanced electrochemical properties of vanadium-doped titanium niobate as a new anode material for lithium-ion batteries. *Electrochim. Acta* **2015**, *186*, 58–63. [CrossRef]
19. Yu, J.X.; He, Y.Y.; Li, J.H.; Dong, C.F.; Dai, Y.X.; Gao, T.T.; Wang, X.; Yue, K.; Zhou, G.W. In-situ rooting biconical-nanorods-like Co-doped FeP@carbon architectures toward enhanced lithium storage performance. *Chem. Eng. J.* **2023**, *477*, 146996. [CrossRef]
20. Zhu, S.; Su, M.H.; Lu, S.Y.; Yang, S.L.; Huang, Y.H.; Mei, J.; Zeng, W.W.; Zhan, H.R.; Liu, Y.Z.; Yang, Y. Enhanced performance of Mo-doped $TiNb_2O_7$ anode material for lithium-ion batteries via KOH sub-molten salt synthesis. *Appl. Surf. Sci.* **2024**, *669*, 160507. [CrossRef]
21. Huang, Y.Z.; Hu, X.; Li, J.W.; Zhang, J.S.; Cai, D.P.; Sa, B.S.; Zhan, H.B.; Wen, Z.H. Rational construction of heterostructured core-shell Bi_2S_3@Co_9S_8 complex hollow particles toward high-performance Li- and Na-ion storage. *Energy Storage Mater.* **2020**, *29*, 121–130. [CrossRef]
22. Cao, L.; Gao, X.W.; Zhang, B.; Ou, X.; Zhang, J.F.; Luo, W.B. Bimetallic sulfide Sb_2S_3@FeS_2 hollow nanorods as high-performance anode materials for sodium-ion batteries. *ACS Nano* **2020**, *14*, 3610–3620. [CrossRef]
23. Li, Y.C.; Zhang, W.Y.; Li, X.N.; Kang, H.W.; Yang, B.C.; Li, Z.K. Facile solvothermal synthesis of Co_{1-x}S@CNTs/AC nanocomposite as integrated electrode for high-performance hybrid supercapacitors. *J. Alloy. Compd.* **2023**, *932*, 167634. [CrossRef]
24. Jo, D.Y.; Park, S.-K. Design of a belt-like single-phase solid-solution Cu-Zn selenide with superior potassium-ion storage properties via a facile cation-exchange process. *Chem. Eng. J.* **2023**, *461*, 142057. [CrossRef]
25. Wang, H.Q.; Zhang, M.; Tan, C.L.; Lai, A.J.; Pan, Q.C.; Zhang, L.X.; Zhong, X.X.; Zheng, F.H.; Huang, Y.G.; Li, Q.Y. Interfacial engineering enables Bi_2S_3@N-doped carbon nanospheres towards high performance anode for lithium-ion batteries. *Electrochim. Acta* **2021**, *398*, 139340. [CrossRef]
26. Dong, Y.C.; Hu, M.J.; Zhang, Z.Y.; Zapien, J.A.; Wang, X.; Lee, J.M. Hierarchical self-assembled Bi_2S_3 hollow nanotubes coated with sulfur-doped amorphous carbon as advanced anode materials for lithium ion batteries. *Nanoscale* **2018**, *10*, 13343–13350. [CrossRef]
27. Ti, Y.M.; Tian, F.H.; Zhang, Q.; Gai, L.H.; Liu, S.J.; Shen, Q. Introduction of as-prepared cobalt source-containing carbon nanotubes to Co_{1-x}S@C mesoporous nanospheres for an ultrahigh lithium storage. *Carbon* **2020**, *165*, 112–121. [CrossRef]
28. Xiu, Z.L.; Huang, B.; Li, X.G.; Yu, J.F.; Meng, X.G.; Ma, J.Y.; Yu, J.X.; Lu, Q.F.; Ji, X.X. Metal-organomecapto complex-derived mesoporous Co_{1-x}S/N, S-codoped carbon composite for superior lithium ion storage. *J. Solid State Chem.* **2022**, *306*, 122770. [CrossRef]
29. Li, B.S.; Wang, R.R.; Chen, Z.L.; Sun, D.L.; Fang, F.; Wu, R.B. Embedding heterostructured MnS/Co_{1-x}S nanoparticles in porous carbon/graphene for superior lithium storage. *J. Mater. Chem. A* **2019**, *7*, 1260. [CrossRef]
30. Zeng, X.Y.; Tang, Y.K.; Liu, L.; Zhang, Y.; Qian, M.; Gao, Y. Carbon nanotube-encapsulated Bi_2S_3 nanorods as electrodes for lithium-ion batteries and lithium-sulfur batteries. *ACS Sustain. Chem. Eng.* **2021**, *9*, 15830–15838. [CrossRef]
31. Zhang, L.X.; Peng, F.; Zhang, M.; Li, D.; Pan, Q.C.; Yang, G.H.; Zheng, F.H.; Huang, Y.G.; Wang, H.Q.; Li, Q.Y. Heterostructured FeS_2/SnS_2 nanoparticles anchored on graphene for advanced lithium and sodium-ion batteries. *Appl. Surf. Sci.* **2022**, *606*, 154864. [CrossRef]
32. Peng, J.H.; Sun, H.H.; Wen, M.Y.; Chen, Y.M.; Luo, Z.X.; Yu, H.Y.; Xue, Y.M.; Wang, J.G. A nanocluster colloidal electrolyte enables highly stable and reversible zinc anodes. *Nano Lett.* **2024**, *24*, 14941–14949. [CrossRef]